

Quantum test of the Universality of Free Fall using rubidium and potassium

H. Albers¹, A. Herbst¹, L. L. Richardson^{1a}, H. Heine¹, D. Nath¹, J. Hartwig¹, C. Schubert¹, C. Vogt², M. Woltmann², C. Lämmerzahl², S. Herrmann², W. Ertmer¹, E. M. Rasel¹, D. Schlippert^{1b}

¹ Leibniz Universität Hannover, Institut für Quantenoptik, Welfengarten 1, 30167 Hannover, Germany

² ZARM Zentrum für angewandte Raumfahrttechnologie und Mikrogravitation, Universität Bremen, Am Fallturm 2, 28359 Bremen, Germany

Received: date / Revised version: date

Abstract. We report on an improved test of the Universality of Free Fall using a rubidium-potassium dual-species matter wave interferometer. We describe our apparatus and detail challenges and solutions relevant when operating a potassium interferometer, as well as systematic effects affecting our measurement. Our determination of the Eötvös ratio yields $\eta_{\text{Rb,K}} = -1.9 \times 10^{-7}$ with a combined standard uncertainty of $\sigma_\eta = 3.2 \times 10^{-7}$.

PACS. 37.25.+k Atom interferometry techniques – 03.75.Dg Atom and neutron interferometry – 06.30.Gv Velocity, acceleration, and rotation

1 Introduction

Matter wave interferometry is an effective toolbox to probe our understanding of nature. Based on coherent manipulation of atomic ensembles, sensors capable of performing accurate inertial measurements have been demonstrated [1–10]. These new atomic sensors allow accessing novel methods to understand fundamental physics [11–15].

The Einstein equivalence principle (EEP) is a cornerstone for the theory of general relativity [16]. It is composed of three components: Local Lorentz Invariance, Local Position Invariance, and the Universality of Free Fall. A violation of any of the components would imply a violation of the EEP and could therefore yield modifications of general relativity with the possibility to reconcile it with quantum field theory and therefore form of a theory of quantum gravity.

The Universality of Free Fall (UFF) states the equality of inertial and gravitational mass $m_{\text{in}} = m_{\text{gr}}$ and implies that all objects freely falling in the same gravitational field experience the same acceleration. As a figure of merit for UFF tests in the Newtonian framework we can express differential acceleration measurements in the so-called Eötvös ratio

$$\eta_{\text{A,B}} \equiv 2 \frac{g_{\text{A}} - g_{\text{B}}}{g_{\text{A}} + g_{\text{B}}} = 2 \frac{\left(\frac{m_{\text{gr}}}{m_{\text{in}}}\right)_{\text{A}} - \left(\frac{m_{\text{gr}}}{m_{\text{in}}}\right)_{\text{B}}}{\left(\frac{m_{\text{gr}}}{m_{\text{in}}}\right)_{\text{A}} + \left(\frac{m_{\text{gr}}}{m_{\text{in}}}\right)_{\text{B}}}, \quad (1)$$

where A and B are the test masses, and $g_{\text{A,B}}$ is their respective local gravitational acceleration.

Tests of the UFF can be grouped in three categories depending on the nature of the test masses: i) classical, ii) semi-classical, and iii) quantum tests as reported in Table 1. The UFF has been tested extensively by classical means, yielding the best uncertainty at parts in 10^{14} . In addition, since the first observation of a gravitationally induced phase in a matter-wave interferometer [17], a variety of quantum tests based on atom interferometry have emerged. Due to their well-defined characteristics, isotopic purity, and by granting access to a novel range of species, they promise high sensitivity to possible violations of the EEP, e.g. when parametrizing observable physics in the minimal Standard Model extension [18–20] or in dilaton coupling scenarios [21].

In this article we report on an improved dual-species test of the Universality of Free Fall using laser-cooled ^{87}Rb and ^{39}K [22]. Improvements are mainly achieved by a better input state preparation for potassium yielding in an increased signal-to-noise ratio and longer integration time. After a description of the experimental apparatus in Sec. 2, we discuss our measurement scheme (Sec. 3) and close with a discussion of systematic effects (Sec. 4) affecting the measurement. In Sec. 5 we present possible mitigation strategies and paths towards improved quantum tests of the UFF on ground [23–26] and in space [27–29].

^a Present address: College of Optical Sciences, University of Arizona, Tucson, AZ 85721, USA

^b Email: schlippert@iqo.uni-hannover.de

Table 1: Overview of UFF tests. We refer to experiments comparing the free fall acceleration of two isotopes of the same (different) chemical species as “dual-isotope” (“dual-species”). Experiments comparing the free fall of different internal states of the same isotope are labelled “dual-state”. FCC – Falling corner cube; AI – Atom interferometer.

Experiment	Test Masses	Type	Eötvös ratio $\eta_{A,B}$	Ref.
Capacitive accelerometers	Ti – Pt	Classical	$-0.1(1.3) \times 10^{-14}$	[30]
Lunar laser ranging	Earth – Moon	Classical	$-3(5) \times 10^{-14}$	[31]
Torsion balance	^9Be – Ti	Classical	$0.3(1.8) \times 10^{-13}$	[32]
Dual-FCC	Cu – U	Classical	$1.3(5.0) \times 10^{-10}$	[33]
FCC vs AI	SiO_2 – ^{133}Cs	Semi-classical	$7(7) \times 10^{-9}$	[34]
FCC vs AI	SiO_2 – ^{87}Rb	Semi-classical	$4.4(6.5) \times 10^{-9}$	[35]
Dual-state AI	^{87}Rb	Quantum	$0.9(2.7) \times 10^{-10}$	[36]
Dual-state AI	^{87}Rb	Quantum	$1.4(2.8) \times 10^{-9}$	[37]
Dual-state AI	^{87}Rb	Quantum	$0.2(1.2) \times 10^{-7}$	[38]
Dual-isotope AI	^{85}Rb – ^{87}Rb	Quantum	$2.8(3.0) \times 10^{-8}$	[39]
Dual-isotope AI	^{85}Rb – ^{87}Rb	Quantum	$1.2(3.2) \times 10^{-7}$	[40]
Dual-isotope AI	^{87}Sr – ^{88}Sr	Quantum	$0.2(1.6) \times 10^{-7}$	[41]
Dual-species AI	^{87}Rb – ^{39}K	Quantum	$-0.3(5.4) \times 10^{-7}$	[22]
Dual-species AI	^{87}Rb – ^{39}K	Quantum	$0.9(3.0) \times 10^{-4}$	[42]
Dual-species AI	^{87}Rb – ^{39}K	Quantum	$-1.9(3.2) \times 10^{-7}$	This work

2 Experimental apparatus

The experimental apparatus includes a vacuum system in which the atoms are interrogated, a laser system generating the light fields for manipulating the atoms, and optics for beam shaping and collecting fluorescence for detection at the vacuum chamber. Below, these elements are described in more detail.

2.1 Vacuum system

The vacuum system consists of three main parts as depicted in Fig. 1 and is enclosed in a single-layer permalloy magnetic shield [43,44]. Cooling and trapping of ^{87}Rb and ^{39}K takes place in a double magneto-optical trap (MOT) setup comprising two custom-made aluminum chambers with indium-sealed viewports separated by a differential pumping tube. Atoms are loaded into the 2D MOT from background vapor generated by ovens heated to 30 °C (75 °C), yielding a partial pressure of 1×10^{-7} mbar (6×10^{-6} mbar) for rubidium (potassium). A tube connects the 3D MOT chamber with a high aperture detection zone, allowing for 200 ms of free fall (19 cm center to center).

2.2 Laser system

For trapping and cooling of both atomic species we use the same laser system as in our previous work [22] and described in detail in [44,45].

In the following we refer to the $|F = 2\rangle \rightarrow |F' = 3\rangle$ as the cooling and the $|F = 1\rangle \rightarrow |F' = 2\rangle$ as the repumping transition. Frequency references for the system are generated by two external cavity diode lasers (ECDL) [46,47]

which are stabilized to the D_2 line of rubidium (potassium) at 780 nm (767 nm) by means of frequency modulation spectroscopy.

The light fields for cooling and repumping of rubidium are generated by two ECDLs in a master-slave configuration. The repumping laser is stabilized to the reference laser and phase locked to be on resonance to the repumping transition. The cooling laser is phase-locked with respect to the repumper with an offset of -3.1Γ from the cooling transition, where $\Gamma \approx 2\pi 6$ MHz is the natural linewidth of rubidium and potassium.

The potassium cooling system consists of three independent ECDLs. For the 2D MOT, one ECDL is phase locked to the reference and detuned by -1.3Γ from the cooling transition. Repumping light is generated by passing this light through a double-pass acousto-optical modulator (AOM) operated at half the hyperfine transition frequency ($f_{\text{HFS}} \approx 461$ MHz). The radio frequency power is set to generate a 50:50 intensity ratio for cooling and repumping light. The repumping light generated with this setup has a detuning of -4Γ from resonance. For the 3D MOT, two independent cooling and repumping lasers are phase locked to the reference laser with a variable detuning to provide the flexibility needed for the potassium sub-Doppler cooling scheme [48].

All generated light fields except the rubidium repumper are amplified using tapered amplifiers (TA), while the intensity is controlled with AOMs. Our setup yields cooling (C) and repumping (RP) intensities at the position of the atoms of $I_C \approx 8 I_{\text{sat}}$, $I_{\text{RP}} \approx 0.1 I_{\text{sat}}$ ($I_C = I_{\text{RP}} \approx 12 I_{\text{sat}}$) for rubidium (potassium), where I_{sat} is each species’s saturation intensity [49,50].

To generate Raman beam splitter light, we utilize two additional ECDLs in master-oscillator power amplification (MOPA) configuration operated as a master-slave pair for each species. A schematic of the utilized system for potassium and the layout for superimposing the light with

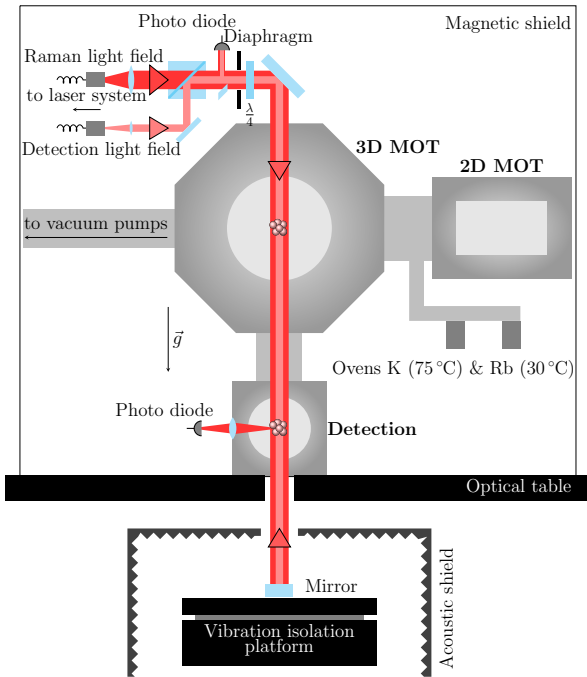


Fig. 1: Schematic of the vacuum system and peripherals comprising the sensor head of the experimental setup. The collimated light for the Raman pulses (dark red) and for detection (light red) are superimposed on a polarizing beam splitter which also cleans the Raman light polarization and allows for correcting detection intensity noise. Downstream, the light is shaped by a diaphragm to suppress reflections and unwanted diffraction from the viewport edge when passing the chamber and is circularly polarized afterwards. A retro-reflection mirror is situated on a vibration isolation platform in an acoustic isolation housing. Fluorescence readout is performed while the atoms fall through the large numerical aperture detection zone.

the rubidium Raman system is depicted in Fig. 2 a). For the rubidium system a similar setup is used. The master lasers are phase locked (PD1) to the reference lasers on the $|F = 1\rangle \rightarrow |F' = 2\rangle$ transition with a global detuning Δ of 3.3 GHz for potassium, and 1.6 GHz for rubidium (cf. Fig. 2 b)). To compensate for the Doppler shift, the slave lasers are phase locked (PD2) with a dynamic detuning δ to the master lasers on the $|F = 2\rangle \rightarrow |F' = 2\rangle$ transition. The beam splitting light fields for both species can be switched independently using AOMs (AOM1 and AOM2 in Fig. 2). A dichroic mirror (DM) is used to superimpose the beam splitting light for both species. Due to the small difference in wavelengths of the D₂ lines of ⁸⁷Rb and ³⁹K, we use common broadband optics at the experiment apparatus. Therefore we are able to generate a spatially and temporally overlapped cold atom cloud as well as superimposed Raman beams.

2.3 Interferometry and detection optics

The Raman beams are set up in a retro-reflected $\sigma^+ - \sigma^+$ polarization configuration. They are collimated to a $1/e^2$ -radius of ~ 1.2 cm using an achromatic lens ($f = 100$ mm) and pass a cleanup polarization beam splitter, where they are superimposed with the detection light (Fig. 1). We obtain powers in the Raman master (slave) beam of 110 mW (110 mW) for potassium and 45 mW (90 mW) for rubidium. Both the detection and the Raman beams pass a diaphragm limiting the beam diameter such that no unwanted diffraction appears at the viewports. A $\lambda/4$ retardation plate generates the circular polarization. The beams are aligned parallel to gravity with two silver-coated mirrors. Below the chamber the beams are retro-reflected by a mirror [Optique Fichou] with a $\lambda/20$ peak-to-valley flatness. This mirror serves as the reference plane of the inertial measurements. To suppress seismic noise, it is mounted on top of a benchtop vibration isolation platform [Minus-K BM-1], and the entire assembly is housed within a foam insulated acoustic isolation box. For state-selective fluorescence detection, we utilize an optical system collecting fluorescence light with a large aperture lens ($f = 50$ mm) and imaging it onto a photo diode [OSI Optoelectronics PIN-10D] in a $2f - 2f$ configuration.

3 Measurements

3.1 Input state preparation

Initially, the atoms are loaded within 1.3 s into the 3D-MOT. Subsequently, the magnetic fields are switched off for the optical molasses to enable sub-Doppler cooling. Following the gray molasses method outlined in Ref. [48] for ³⁹K and standard sub-Doppler cooling techniques for ⁸⁷Rb we typically obtain 5×10^8 (6×10^7) atoms at a temperature of 21 μ K (28 μ K) for rubidium (potassium) within 15 ms. Due to the trade-off in molasses temperature in favor of ³⁹K, the temperature of ⁸⁷Rb is higher than the typical value of 8 μ K when optimizing for ⁸⁷Rb only.

The procedure described in the following combines a state preparation with a vertical velocity selection for an increased signal-to-noise ratio [51, 52]. Subsequent to the sub-Doppler cooling the atoms are optically pumped into the $|F = 1, m_F\rangle$ manifold. Afterwards they are released into free fall. A quantization field of $B_0 = 500$ mG is applied to lift the degeneracy of the magnetic sub-levels as depicted in a Raman resonance spectrum in Fig. 3. A microwave pulse transfers the atoms from the $|F = 1, m_F = 0\rangle$ into the $|F = 2, m_F = 0\rangle$ state. The microwave transitions are realized using a Yagi-Uda type antenna for potassium and a loop antenna for rubidium. Then, the $|F = 1\rangle$ state is depopulated by optically pumping the remaining atoms into the $|F = 2\rangle$ manifold with an equal distribution. This results in a population of the $|F = 2, m_F = 0\rangle$ state with up to 45 % of the atoms [52]. After a time of flight of 44 ms accommodating these steps, a velocity-selective Raman pulse selects a narrow vertical velocity class [53] of atoms

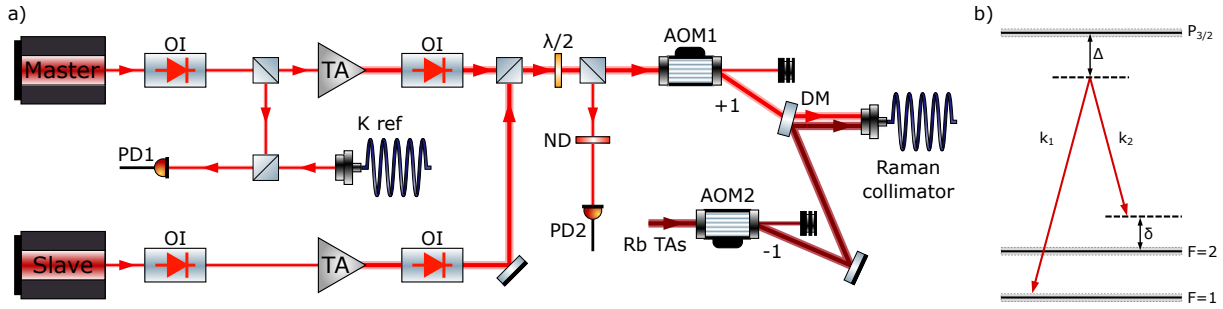


Fig. 2: a) Schematic of the potassium Raman laser system (light red) and the superposition with the rubidium Raman laser light (dark red). Two ECDLs in a master-slave configuration are used for each species. The master laser is offset locked (PD1) to the reference laser, while the slave laser is locked against the master (PD2). Both beams are amplified using tapered amplifiers and can be switched with an AOM. b) Level scheme of the Raman transition. A global detuning Δ is used for both lasers with an additional, variable detuning δ for the slave laser. Abbreviations: OI – Optical isolator, TA – Tapered amplifier, AOM – Acousto-optical modulator, PD – Photo diode, DM – Dichroic mirror, ND – Neutral density filter.

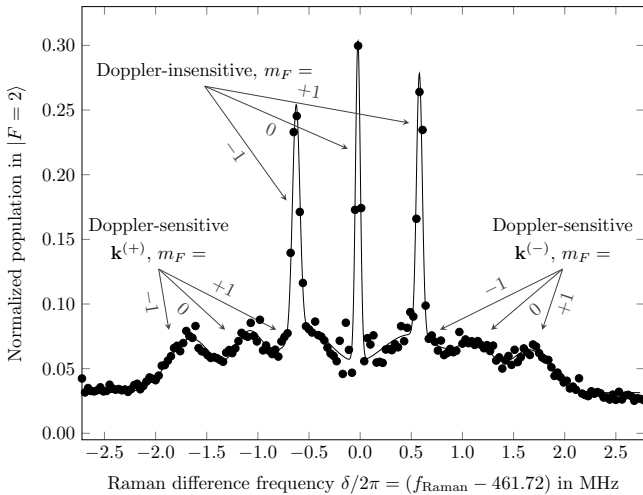


Fig. 3: Typical potassium Raman resonance spectrum obtained by scanning δ and applying single Raman pulses. The spectrum is acquired at the following parameters: pulse width $\tau = 15 \mu\text{s}$, offset field $B_0 = 430 \text{ mG}$, time of flight $t_{\text{TOF}} = 43.25 \text{ ms}$, temperature $T = 32.6 \mu\text{K}$. The solid black line is a guide to the eye. In the retro-reflected setup using σ/σ -polarization, a total of nine resonances are visible, three of which form one subset of Doppler-insensitive transitions. The remaining two subsets of three Doppler-sensitive transitions each are labeled $k^{(+)}$ for upward and $k^{(-)}$ for downward momentum transfer. Figure modified from Ref. [45].

from the $|F = 2, m_F = 0\rangle$ state by transferring them into the $|F = 1, m_F = 0\rangle$ state. The remaining atoms from the $|F = 2\rangle$ manifold are removed by a light pulse addressing the cooling transition, concluding the preparation sequence.

3.2 Mach-Zehnder atom interferometry

Atom interferometry is performed simultaneously with both species using the atomic sources described in Sec. 3.1. We employ two-photon Raman transitions [54] driven by counter-propagating beams with wave vectors $k_i = 2\pi/\lambda_i$, where λ_i refers to the D_2 transition wavelength. The index i indicates the species ^{87}Rb and ^{39}K . We form a Mach-Zehnder-type atom interferometer with a $\pi/2 - \pi - \pi/2$ pulse sequence separated by free evolution times T to coherently split, reflect, and recombine the wavepackets. The atomic recoil $\Delta p \approx 2\hbar k_i = \hbar k_{\text{eff},i}$ induced by atom-light interaction leads to a finite space-time area enclosed by the AI (Fig. 4). For our scale factors, the presence of our commercial vibration isolation platform allows us to scan fringes as opposed to using an ellipse fitting algorithm commonly used in differential atom interferometers [55–57].

The population of the output ports of the interferometer depends on the accumulated phase difference $\Delta\phi$ between the two paths of the interferometer [34, 58, 59] and is given by:

$$P_{|F=2\rangle} = A \cdot \cos(\Delta\phi) + P_0, \quad (2)$$

where $P_{|F=2\rangle}$ is the fraction of atoms in the excited $|F = 2\rangle$ state, $C = A/P_0$ is the contrast, and P_0 the offset. The population is measured by a normalized state selective fluorescence detection, within which the pulses reading out potassium are nested within the rubidium detection sequence.

The leading order phase shift of such an interferometer due to an acceleration¹ a_i in the direction of beam splitting reads [34, 58, 59]

$$\Delta\phi = k_{\text{eff},i} a_i T^2. \quad (3)$$

¹ If derived from the Schrödinger equation with masses m_{in} in the kinetic term and m_{gr} in the Newtonian potential, a prefactor resembling those in Eq. 1, $a_i \rightarrow \frac{m_{\text{gr}}}{m_{\text{in}}} a_i$ becomes apparent.

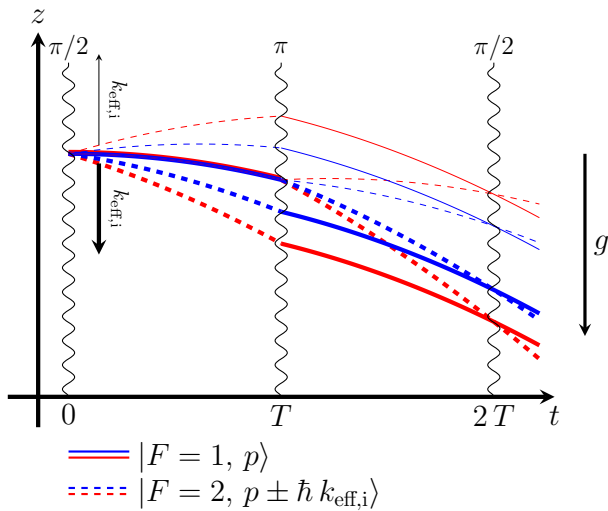


Fig. 4: Space-time diagram of a dual-species Mach-Zehnder matter-wave interferometer in a constant gravitational field for the downward (thick lines) and upward (thin lines) direction of momentum transfer. Stimulated Raman transitions at times 0 , T , and $2T$ couple the states $|F_i = 1, p\rangle$ (solid lines) and $|F_i = 2, p \pm \hbar k_{\text{eff},i}\rangle$ (dashed lines), where i stands for Rb (blue lines) or K (red lines). The velocity change induced by the Raman pulses is not to scale with respect to the gravitational acceleration.

Applying a phase-continuous frequency ramp α_i not only maintains the Raman resonance condition under the influence of a gravitational Doppler shift, but also mimics an effective acceleration of the Raman wave fronts

$$a_i = \frac{\alpha_i}{k_{\text{eff},i}} \quad (4)$$

and accordingly enters the phase shift as follows:

$$\Delta\phi_i = (g_i - \frac{\alpha_i}{k_{\text{eff},i}}) \cdot k_{\text{eff},i} \cdot T^2. \quad (5)$$

For $\alpha_i = k_{\text{eff},i} \cdot g_i$ the accumulated phase shift $\Delta\phi_i = 0$ for all pulse separation times T .

We apply the momentum reversal technique [51, 60] to suppress systematic errors independent of the direction of momentum transfer. We distinguish two types of undesired phase perturbations, k -dependent ($\delta\phi_{\text{dep}}$) and k -independent ($\delta\phi_{\text{ind}}$) shifts. In our setup, the two possible counter-propagating Raman beam configurations have opposite effective wave vectors and allow for selecting the direction of momentum transfer. We label these particular transitions as $\mathbf{k}^{(+)}$ and $\mathbf{k}^{(-)}$ (Fig. 3). The phase shifts in $\mathbf{k}^{(+)}$ and $\mathbf{k}^{(-)}$ configuration can be written as:

$$\Delta\phi_+ = k_{\text{eff}} a T^2 + \delta\phi_{\text{ind}} + \delta\phi_{\text{dep}} \quad (6)$$

$$\Delta\phi_- = -k_{\text{eff}} a T^2 + \delta\phi_{\text{ind}} - \delta\phi_{\text{dep}} \quad (7)$$

Consequently, their phase difference is given by:

$$\Delta\phi_{\text{tot}} = \frac{\Delta\phi_+ - \Delta\phi_-}{2} = k_{\text{eff}} a T^2 + \delta\phi_{\text{dep}}. \quad (8)$$

Hence, by alternating the direction of momentum transfer we can largely suppress momentum independent ($\delta\phi_{\text{ind}}$) systematic effects, e.g. the AC-Stark shift, with dynamics slower than a typical momentum reversal sequence as described in the following subsection.

3.3 Obtaining the Eötvös ratio

The gravitational accelerations g_i (Eq. 5) are determined through the central fringe positions $a_i^{(\pm)}(g)$. For determining the latter, we operate both interferometers at three pulse separation times $T = 35, 38, 41$ ms. Fig. 5 displays scans around the respective $a_i^{(\pm)}(g)$. Here, for the downward direction of momentum transfer the sign of the phase shift is inverted in order to yield a positive value $g_i > 0$.

We then operate both interferometers simultaneously around their central fringe positions with $T = 41$ ms. To this end we scan across the central fringe positions in 10 steps and alternate the direction of momentum transfer afterwards. This procedure constitutes a single measurement cycle with a duration of 32 s (2×10 shots). Each measurement cycle yields g_{Rb} and g_{K} , allowing us to compute an Eötvös ratio (Eq. 1).

4 Data analysis and results

4.1 Statistical analysis

We acquire 30000 shots over consecutive 13 hours. This is limited by technical circumstances related to the stability of the laser locks. Fig. 6 shows the normalized Allan deviation of our measurement which yields an instability $\sigma_\eta = 9 \times 10^{-8}$ after 8192 s integration time. This instability is fully dominated by the potassium interferometer due to its larger technical noise influence stemming mainly from the detection at a significantly lower contrast (Fig. 5). The latter can be explained by the underlying large transverse expansion rate of potassium and related homogeneous excitation when the ensemble diameter becomes comparable to the Raman beam diameter.

4.2 Systematic effects

Table 2 lists the systematic effects that are not suppressed by the momentum reversal method. Here, the analysis follows Refs. [60–65] with the following assumptions for Rb (K): Temperature – 21 μK (28 μK) with a 10 % uncertainty; Initial size – 1 mm (1 mm); π -pulse width – 15 μs (15 μs); Free evolution time – 41 ms (41 ms); Time-of-flight prior to the 1st interferometry pulse – 54.5 ms; Differential center-of-mass (COM) position uncertainty in z – 1 mm; Differential COM velocity uncertainty in z – 1 mm/s.

Below we discuss the treatment of the dominant systematic contributions originating from stray magnetic fields and wave front aberration.

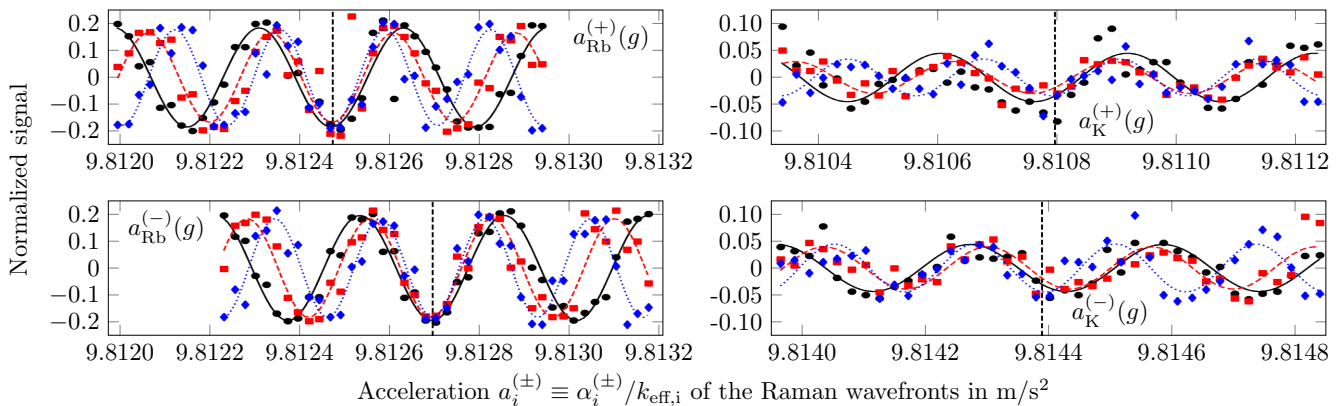


Fig. 5: Determination of the differential gravitational acceleration of rubidium (left) and potassium (right). Typical fringe signals and sinusoidal fit functions are plotted in dependence of the effective Raman wave front acceleration for pulse separation times $T = 35$ ms (black circles and solid black line), $T = 38$ ms (red squares and dashed blue line), and $T = 41$ ms (blue diamonds and dotted red line) for upward (+) and downward (-) direction of momentum transfer. The central fringe positions $a_i^{(\pm)}(g)$, $i = \text{Rb}, \text{K}$ for $T = 41$ ms are marked with dashed vertical lines. The data sets are corrected for slow linear drifts caused by varying offsets in the detection and global signal offsets.

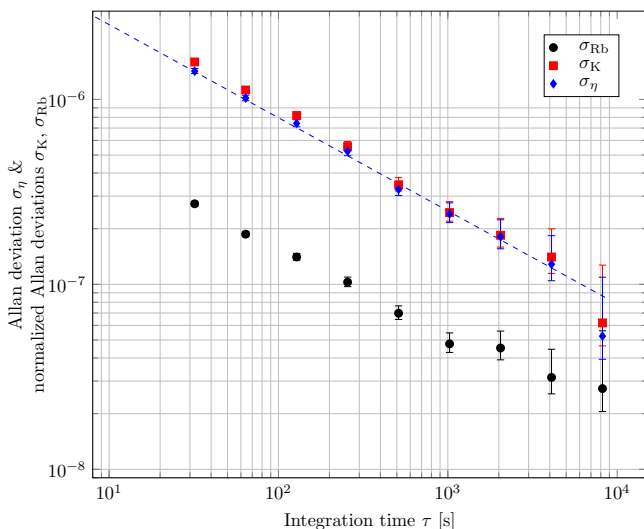


Fig. 6: Normalized Allan deviations σ_{Rb} , σ_{K} , and the Allan deviation σ_η of the signals providing us with the accelerations g_{Rb} and g_{K} of rubidium (black circles) potassium (red squares), and of the Eötvös ratio $\eta_{\text{Rb},\text{K}}$ (blue diamonds) in their dependence of the integration time τ . Using a fit $\propto 1/\sqrt{\tau}$ (blue dashed line) we extract a statistical uncertainty of the Eötvös ratio of $\sigma_\eta = 9 \times 10^{-8}$ after 8192 s integration. The measurement is solely limited by the stability of the potassium signal.

4.2.1 Zeeman effect

Magnetic fields along the interferometric trajectories change each respective species's hyperfine transition frequency. Due to state preparation into the $|F = 1, m_F = 0\rangle$ magnetically insensitive state the Zeeman effect cancels to

Table 2: Estimated bias contributions for the $\eta_{\text{Rb},\text{K}}$ ratio and their uncertainties σ . We estimate the uncertainties to be uncorrelated at the discussed level of accuracy.

Contribution	Correction $\Delta\eta$	Uncertainty $\delta\eta$
Zeeman effect	-1.3×10^{-6}	6.0×10^{-8}
Wave front aberration	0	3×10^{-7}
Coriolis force	0	9×10^{-9}
2-photon light shift	3.08×10^{-8}	6×10^{-10}
Effective wave vector	0	1.3×10^{-9}
1 st order gravity gradient	0	1×10^{-10}
Total bias	-1.28×10^{-6}	3.1×10^{-7}

first order. However spatial and temporal variations of the magnetic field along the axis of interferometry contribute a non-zero bias phase resulting from the remaining clock shift affecting atoms in $m_F = 0$.

Magnetic fields shift the hyperfine transition frequency by $\Delta\omega_{\text{clock}}^i = 2\pi\kappa^i \cdot B^2$, where $\kappa^{\text{Rb}} = 575.15 \text{ Hz/G}^2$ for ^{87}Rb , and $\kappa^{\text{K}} = 8.5 \text{ kHz/G}^2$ for ^{39}K . Based on a characterization using Raman spectroscopy at different positions along the vertical axis we can model the magnetic field as

$$B(z(t), t) = B_0(t) + \frac{\partial B}{\partial z} \cdot z_{\text{COM}}(t) \quad (9)$$

where $B_0(t)$ describes the temporal behaviour of the bias field due to the switching behaviour of the respective power supply², and $z_{\text{COM}}(t)$ is the free fall center of mass motion of the atoms defined as: $z_{\text{COM}}(t) = z_0 + (v_0 \pm v_{\text{rec}}/2) \cdot t + 1/2at^2$ with z_0 being the initial position of the atoms, v_0 the velocity, and v_{rec} the recoil velocity defined as $v_{\text{rec}} = \hbar k_{\text{eff}}/m$. Only the recoil velocity is dependent on the direc-

² We have characterized the switch-on to be saturating at 500 mG with a time constant of 90 ms.

tion of momentum transfer, and therefore all other components are suppressed by k -reversal. Using the sensitivity function formalism [66] we can calculate the frequency shifts

$$\Delta\omega_{Z(\pm),i}(t) \equiv \pm 2\pi\kappa^i \cdot \frac{\partial B}{\partial z} \cdot B(t) \cdot v_{\text{rec},i} t, \quad (10)$$

with the clock shift $\Delta\omega_{\text{clock},i}$. Computing the integral of the clock shift weighted with the sensitivity function $g_s(t)$

$$\Delta\Phi_i^Z \equiv \int_{-\infty}^{\infty} g_s(t) \Delta\omega_{Z(\pm),i}(t) dt \quad (11)$$

allows deriving the bias due to the Zeeman effect. With a gradient $\frac{\partial B}{\partial z} = 3 \text{ mG/cm}$ and using the sensitivity formalism for rubidium and potassium the inferred bias affecting the Eötvös ratio amounts to $-1.30(0.06) \times 10^{-6}$. We note that the resulting bias was also confirmed using a perturbation theory formalism [67].

4.2.2 Wave front aberration

Our estimation of systematic uncertainty owing to wave front aberration is based on numerical simulation. To this end, we take into account the Raman light fields' propagation including curvatures of view ports and the retro-reflection mirror, uncertainty in the positioning of the collimation lens, and differential ensemble expansion. In 10^4 trials, we randomly vary these parameters as follows and calculate the resulting phase contribution [63]: For the top and bottom view port curvatures ($\lambda/10$) and the retro-reflection mirror ($\lambda/20$) we assume uncertainties of 10%, for the positioning of the collimation lens we assume an uncertainty of 0.1% and the ensemble temperatures are varied with an uncertainty of 10%. Statistical analysis then yields an uncertainty in the Eötvös ratio of 3×10^{-7} due to wave front aberration.

4.3 Summary & discussion

We determine an Eötvös ratio of $\eta_{\text{Rb,K}} = -1.9 \times 10^{-7}$ with a combined (statistical and systematic) standard uncertainty of 3.2×10^{-7} , constituting about a factor of two improvement over our previous result [22]. We estimate a contribution of the statistical uncertainty of 9×10^{-8} and the systematic uncertainty of 3.1×10^{-7} .

Increased free fall times in comparison to our previous result [22] lead to larger systematic error contributions, e.g., due to the distance traveled through the magnetic field gradient which yields an increased correction, and more challenging characterization of it resulting in a larger uncertainty. The increase in the contribution from wave front aberration is caused by a more defensive modeling of all relevant optical components.

5 Conclusion & outlook

We reported on a test of the UFF with our dual atom interferometer operating simultaneously with ^{87}Rb and ^{39}K . The result of our measurement of the Eötvös parameter is $-1.9(3.2) \times 10^{-7}$ with the lowest uncertainty in an atom interferometer with two different chemical elements reported so far. It corresponds to an improvement of a factor of two with respect to our previous result which we attribute to an improved state preparation of the ^{39}K ensemble. Our analysis shows that the intrinsic noise of the ^{39}K interferometer limits the statistical uncertainty. The reasons are the residual transverse expansion rate implying imperfections in the coherent excitation leading to a reduction in contrast. Among the systematic effects, we identify the inhomogeneity in the magnetic bias field and wave front aberration as the main contributors.

Advanced cooling techniques such as evaporation in an optical dipole trap [68] are expected to enhance the contrast [69,70] and will allow us to reduce wave front-related errors by achieving colder temperatures and by tuning the differential expansion of the two species. The homogeneity of the magnetic field can be improved by an upgrade of the magnetic shield [71], a more in-depth characterization, and advanced center-of-mass control over the ensembles. By relying on the differential suppression of vibration noise between the two elements [57] we envisage the perspective for a test on the level of 10^{-9} .

To date, the universality of free fall has proven to be successful with no precision test uncovering a significant deviation. Atom interferometers add a complementary approach to the toolbox for these tests. Compared to the best classical tests (Table 1), this still represents a modest result, but further enhancements are possible and realistic. Using evaporated atoms and matter-wave collimation techniques [72–74] opens the pathway to upgrade the beam splitters to hundreds of coherent photon momentum kicks [75–82] and extended free evolution times on the order of seconds. Very long baseline atom interferometers relying on these techniques promise to venture beyond 10^{-13} [23–26]. In parallel, microgravity research investigates the benefits and the adaption of atom interferometers to operation in drop tower experiments [74, 83, 84], on a sounding rocket [85], the international space station [28, 86], and dedicated satellite missions [27, 29] with the target of 10^{-15} and beyond.

6 Acknowledgments

We are grateful to É. Wodey, H. Ahlers, and B. Barrett for discussions and critical proof reading of the manuscript, and T. Hensel for careful cross checks concerning the systematic error originating from magnetic fields. This project is supported by the German Space Agency (DLR) with funds provided by the Federal Ministry for Economic Affairs and Energy (BMWi) due to an enactment of the German Bundestag under Grant No. DLR 50WM1641 (PRIMUS-III). The authors furthermore acknowledge financial support by the German Science Foundation (DFG)

through the Collaborative Research Centers 1128 “geo-Q” (projects A02 and F01), 1227 “DQ-mat” (project B07), the Deutsche Forschungsgemeinschaft (DFG, German Research Foundation) under Germanys Excellence Strategy EXC-2123 QuantumFrontiers 390837967 (research unit B02), “Niedersächsisches Vorab” through the “Quantum- and NanoMetrology” (QUANOMET) initiative within the project QT3, and “Wege in die Forschung (II)” of Leibniz Universität Hannover. A.H. and D.S. gratefully acknowledge funding by the Federal Ministry of Education and Research (BMBF) through the funding program Photonics Research Germany under contract number 13N14875.

7 Authors contributions

W.E., E.M.R., C.S., J.H., and D.S. designed the atom interferometer and its laser system. L.L.R., H.A., D.N., J.H., and D.S. contributed to the design of the atom interferometer and its laser system and realised the overall setup. H.A., L.L.R., H.H., and D.N. operated the final experimental setup. H.A., A.H., D.S., J.H., C.S., and H.H. performed the analysis of the data presented in this manuscript. D.S., H.A., L.L.R., C.S., and A.H. drafted the initial manuscript. C.V., M.W., C.L., and S.H. provided major input to the manuscript and all authors critically reviewed and approved of the final version.

References

1. J. K. Stockton, K. Takase, and M. A. Kasevich. Absolute geodetic rotation measurement using atom interferometry. *Phys. Rev. Lett.*, 107:133001, 2011.
2. Vincent Mnoiret, Pierre Vermeulen, Nicolas Le Moigne, Sylvain Bonvalot, Philippe Bouyer, Arnaud Landragin, and Bruno Desruelle. Gravity measurements below 10⁻⁹ g with a transportable absolute quantum gravimeter. *Scientific Reports*, 8(1):12300, August 2018.
3. Zhong-Kun Hu, Bu-Liang Sun, Xiao-Chun Duan, Min-Kang Zhou, Le-Le Chen, Su Zhan, Qiao-Zhen Zhang, and Jun Luo. Demonstration of an ultrahigh-sensitivity atom-interferometry absolute gravimeter. *Phys. Rev. A*, 88:043610, Oct 2013.
4. D. Savoie, M. Altorio, B. Fang, L. A. Sidorenkov, R. Geiger, and A. Landragin. Interleaved atom interferometry for high-sensitivity inertial measurements. *Science Advances*, 4:eaau7948, 2018.
5. C Freier, M Hauth, V Schkolnik, B Leykauf, M Schilling, H Wziontek, H-G Scherneck, J Müller, and A Peters. Mobile quantum gravity sensor with unprecedented stability. *Journal of Physics: Conference Series*, 723(1):012050, 2016.
6. P. Berg, S. Abend, G. Tackmann, C. Schubert, E. Giese, W. P. Schleich, F. A. Narducci, W. Ertmer, and E. M. Rasel. Composite-light-pulse technique for high-precision atom interferometry. *Phys. Rev. Lett.*, 114:063002, Feb 2015.
7. F. Sorrentino, A. Bertoldi, Q. Bodart, L. Cacciapuoti, M. de Angelis, Y.-H. Lien, M. Prevedelli, G. Rosi, and G. M. Tino. Simultaneous measurement of gravity acceleration and gravity gradient with an atom interferometer. *Applied Physics Letters*, 101(11):114106, 2012.
8. Y. Bidel, N. Zahzam, C. Blanchard, A. Bonnin, M. Cadoret, A. Bresson, D. Rouxel, and M. F. Lequentrec-Lalancette. Absolute marine gravimetry with matter-wave interferometry. *Nature Communications*, 9(1):627, February 2018.
9. R. Geiger, V. Mnoiret, G. Stern, N. Zahzam, P. Cheinet, B. Battelier, A. Villing, F. Moron, M. Lours, Y. Bidel, A. Bresson, A. Landragin, and P. Bouyer. Detecting inertial effects with airborne matter-wave interferometry. *Nature Communications*, 2(1):474, September 2011.
10. Yannick Bidel, Nassim Zahzam, Alexandre Bresson, Cdric Blanchard, Malo Cadoret, Arne V. Olesen, and Ren Forsberg. Absolute airborne gravimetry with a cold atom sensor. *Journal of Geodesy*, 94(2):20, January 2020.
11. G Rosi, F Sorrentino, L Cacciapuoti, M Prevedelli, and GM Tino. Precision measurement of the newtonian gravitational constant using cold atoms. *Nature*, 510(7506):518–521, 2014.
12. Matt Jaffe, Philipp Haslinger, Victoria Xu, Paul Hamilton, Amol Upadhye, Benjamin Elder, Justin Houry, and Holger Müller. Testing sub-gravitational forces on atoms from a miniature in-vacuum source mass. *Nature Physics*, 13:938–, July 2017.
13. Philipp Haslinger, Matt Jaffe, Victoria Xu, Osip Schwartz, Matthias Sonnleitner, Monika Ritsch-Marte, Helmut Ritsch, and Holger Müller. Attractive force on atoms due to blackbody radiation. *Nature Physics*, 14:–, 2017.
14. Rym Bouchendira, Pierre Cladé, Saïda Guellati-Khélifa, François Nez, and François Biraben. New determination of the fine structure constant and test of the quantum electrodynamics. *Phys. Rev. Lett.*, 106:080801, Feb 2011.
15. Richard H. Parker, Chenghui Yu, Weicheng Zhong, Brian Estey, and Holger Müller. Measurement of the fine-structure constant as a test of the standard model. *Science*, 360(6385):191–195, 2018.
16. Clifford M. Will. The confrontation between general relativity and experiment. *Living Reviews in Relativity*, 9(3):–, 2006.
17. R. Colella, A. W. Overhauser, and S. A. Werner. Observation of gravitationally induced quantum interference. *Phys. Rev. Lett.*, 34(23):1472–1474, June 1975.
18. V. Alan Kostelecký and Jay D. Tasson. Matter-gravity couplings and lorentz violation. *Phys. Rev. D*, 83:016013, Jan 2011.
19. Michael A. Hohensee, Holger Müller, and R. B. Wiringa. Equivalence principle and bound kinetic energy. *Phys. Rev. Lett.*, 111(15):151102–, October 2013.
20. Holger Mueller. Quantum mechanics, matter waves, and moving clocks. [arXiv:1312.6449](https://arxiv.org/abs/1312.6449).
21. Thibault Damour. Theoretical aspects of the equivalence principle. *Classical and Quantum Gravity*, 29(18):184001, 2012.
22. D. Schlippert, J. Hartwig, H. Albers, L. L. Richardson, C. Schubert, A. Roura, W. P. Schleich, W. Ertmer, and E. M. Rasel. Quantum test of the universality of free fall. *Phys. Rev. Lett.*, 112:203002, May 2014.
23. S. Dimopoulos, P. W. Graham, J. M. Hogan, and M. A. Kasevich. Testing general relativity with atom interferometry. *Phys. Rev. Lett.*, 98(11):111102–, 2007.
24. C. Overstreet, P. Asenbaum, T. Kovachy, R. Notermans, J. M. Hogan, and M. A. Kasevich. Matter wave lensing to picokelvin temperatures. *Phys. Rev. Lett.*, 120:183604, 2018.

25. L. Zhou et al. Development of an atom gravimeter and status of the 10-meter atom interferometer for precision gravity measurement. *General Relativity and Gravitation*, 43(7):1931–1942–, 2011.
26. J Hartwig, S Abend, C Schubert, D Schlippert, H Ahlers, K Posso-Trujillo, N Gaaloul, W Ertmer, and E M Rasel. Testing the universality of free fall with rubidium and ytterbium in a very large baseline atom interferometer. *New Journal of Physics*, 17(3):035011, 2015.
27. D N Aguilera, H Ahlers, B Battelier, A Bawamia, A Bertoldi, R Bondarescu, K Bongs, P Bouyer, C Braxmaier, L Cacciapuoti, C Chaloner, M Chwalla, W Ertmer, M Franz, N Gaaloul, M Gehler, D Gerardi, L Gesa, N Gürlebeck, J Hartwig, M Hauth, O Hellmig, W Herr, S Herrmann, A Heske, A Hinton, P Ireland, P Jetzer, U Johann, M Krutzik, A Kubelka, C Lämmerzahl, A Landragin, I Lloro, D Massonnet, I Mateos, A Milke, M Nofrarias, M Oswald, A Peters, K Posso-Trujillo, E Rasel, E Rocco, A Roura, J Rudolph, W Schleich, C Schubert, T Schuldt, S Seidel, K Sengstock, C F Sopena, F Sorrentino, D Summers, G M Tino, C Trenkel, N Uzunoglu, W von Klitzing, R Walsler, T Wendrich, A Wenzlawski, P Weels, A Wicht, E Wille, M Williams, P Windpassinger, and N Zahzam. Ste-questtest of the universality of free fall using cold atom interferometry. *Classical and Quantum Gravity*, 31(11):115010, 2014.
28. J. Williams, S.-w. Chiow, N. Yu, and H. Müller. Quantum test of the equivalence principle and space-time aboard the international space station. *New J. Phys.*, 18(2):025018, 2016.
29. J. Bergé *et al.*. Exploring the foundations of the universe with space tests of the equivalence principle. [arXiv:1908.11785](https://arxiv.org/abs/1908.11785), 2019.
30. Pierre Touboul, Gilles Métris, Manuel Rodrigues, Yves André, Quentin Baghi, Joël Bergé, Damien Boulanger, Stefanie Bremer, Patrice Carle, Ratana Chhun, Bruno Christophe, Valerio Cipolla, Thibault Damour, Pascale Danto, Hansjoerg Dittus, Pierre Fayet, Bernard Foulon, Claude Gageant, Pierre-Yves Guidotti, Daniel Hagedorn, Emilie Hardy, Phuong-Anh Huynh, Henri Inchauspe, Patrick Kayser, Stéphanie Lala, Claus Lämmerzahl, Vincent Lebat, Pierre Leseur, Fran çoise Liorzou, Meike List, Frank Löffler, Isabelle Panet, Benjamin Pouilloux, Pascal Prieur, Alexandre Rebray, Serge Reynaud, Benny Rievers, Alain Robert, Hanns Selig, Laura Serron, Timothy Sumner, Nicolas Tanguy, and Pieter Visser. Microscope mission: First results of a space test of the equivalence principle. *Phys. Rev. Lett.*, 119:231101, Dec 2017.
31. F Hofmann and J Müller. Relativistic tests with lunar laser ranging. *Classical and Quantum Gravity*, 35(3):035015, 2018.
32. S. Schlamminger, K.-Y. Choi, T. A. Wagner, J. H. Gundlach, and E. G. Adelberger. Test of the equivalence principle using a rotating torsion balance. *Phys. Rev. Lett.*, 100:041101, Jan 2008.
33. T. M. Niebauer, M. P. McHugh, and J. E. Faller. Galilean test for the fifth force. *Phys. Rev. Lett.*, 59:609–612, Aug 1987.
34. A. Peters, K. Y. Chung, and S. Chu. Measurement of gravitational acceleration by dropping atoms. *Nature*, 400:849–852, August 1999.
35. S Merlet, Q Bodart, N Malossi, A Landragin, F Pereira Dos Santos, O Gitlein, and L Timmen. Comparison between two mobile absolute gravimeters: optical versus atomic interferometers. *Metrologia*, 47(4):L9, 2010.
36. Ke Zhang, Min-Kang Zhou, Yuan Cheng, Le-Le Chen, Qin Luo, Wen-Jie Xu, Lu-Shuai Cao, Xiao-Chun Duan, and Zhong-Kun Hu. Testing the universality of free fall at 10^{-10} level by comparing the atoms in different hyperfine states with bragg diffraction.
37. G. Rosi, G. D’Amico, L. Cacciapuoti, F. Sorrentino, M. Prevedelli, M. Zych, . Brukner, and G. M. Tino. Quantum test of the equivalence principle for atoms in coherent superposition of internal energy states. *Nature Communications*, 8:15529, 2017.
38. Xiao-Chun Duan, Xiao-Bing Deng, Min-Kang Zhou, Ke Zhang, Wen-Jie Xu, Feng Xiong, Yao-Yao Xu, Cheng-Gang Shao, Jun Luo, and Zhong-Kun Hu. Test of the universality of free fall with atoms in different spin orientations. *Phys. Rev. Lett.*, 117:023001, Jul 2016.
39. Lin Zhou, Shitong Long, Biao Tang, Xi Chen, Fen Gao, Wencui Peng, Weitao Duan, Jiaqi Zhong, Zongyuan Xiong, Jin Wang, Yuanzhong Zhang, and Mingsheng Zhan. Test of equivalence principle at 10^{-8} level by a dual-species double-diffraction raman atom interferometer. *Phys. Rev. Lett.*, 115:013004, Jul 2015.
40. A. Bonnin, N. Zahzam, Y. Bidet, and A. Bresson. Simultaneous dual-species matter-wave accelerometer. *Phys. Rev. A*, 88(4):043615, October 2013.
41. M. G. Tarallo, T. Mazzoni, N. Poli, D. V. Sutyryn, X. Zhang, and G. M. Tino. Test of Einstein Equivalence Principle for 0-Spin and Half-Integer-Spin Atoms: Search for Spin-Gravity Coupling Effects. *Physical Review Letters*, 113(2):023005, July 2014.
42. Brynle Barrett, Laura Antoni-Micollier, Laure Chichet, Baptiste Battelier, Thomas Lévque, Arnaud Landragin, and Philippe Bouyer. Dual matter-wave inertial sensors in weightlessness. *Nature Communications*, 7:13786, 2016.
43. Maic Zaiser. *Eine Quelle quantenentarteter Gase fr die Atominterferometrie*. Phd thesis, Leibniz Universität Hannover, 2010.
44. J.M. Hartwig. *Analyse eines atomaren Gravimeters hinsichtlich eines Quantentests des Äquivalenzprinzips*. Phd thesis, Leibniz Universität Hannover, 2013.
45. D. Schlippert. *Quantum test of the Universality of Free Fall*. Phd thesis, Leibniz Universität Hannover, 2014.
46. X. Baillard, A. Gauguet, S. Bize, P. Lemonde, Ph. Laurent, A. Clairon, and P. Rosenbusch. Interference-filter-stabilized external-cavity diode lasers. *Optics Communications*, 266(2):609 – 613, 2006.
47. M. Gilowski, Ch. Schubert, M. Zaiser, W. Herr, and T. W. Narrow bandwidth interference filter-stabilized diode laser systems for the manipulation of neutral atoms. *Optics Communications*, 280(2):443 – 447, 2007.
48. M. Landini, S. Roy, L. Carcagnì, D. Trypogeorgos, M. Fattori, M. Inguscio, and G. Modugno. Sub-doppler laser cooling of potassium atoms. *Phys. Rev. A*, 84:043432, Oct 2011.
49. D. A. Steck. Rubidium 87 d line data. *Rubidium 87 D line data*, 2015.
50. T. G. Tiecke. *Properties of potassium*. *Properties of Potassium*, 2019.
51. J. M. McGuirk, G. T. Foster, J. B. Fixler, M. J. Snadden, and M. A. Kasevich. Sensitive absolute-gravity gradiometry using atom interferometry. *Phys. Rev. A*, 65:033608, Feb 2002.

52. L. Antoni-Micollier, B. Barrett, L. Chichet, G. Condon, B. Battelier, A. Landragin, and P. Bouyer. Generation of high-purity low-temperature samples of ^{39}K for applications in metrology. *Phys. Rev. A*, 96:023608, Aug 2017.
53. Mark Kasevich, David S. Weiss, Erling Riis, Kathryn Moler, Steven Kasapi, and Steven Chu. Atomic velocity selection using stimulated raman transitions. *Phys. Rev. Lett.*, 66:2297–2300, May 1991.
54. Mark Kasevich and Steven Chu. Atomic interferometry using stimulated raman transitions. *Phys. Rev. Lett.*, 67:181–184, Jul 1991.
55. G Varoquaux, R A Nyman, R Geiger, P Cheinet, A Landragin, and P Bouyer. How to estimate the differential acceleration in a two-species atom interferometer to test the equivalence principle. *New Journal of Physics*, 11(11):113010, nov 2009.
56. Xi Chen, Jiaqi Zhong, Hongwei Song, Lei Zhu, Jin Wang, and Mingsheng Zhan. Proportional-scanning-phase method to suppress the vibrational noise in non-isotope dual-atom-interferometer-based weak-equivalence-principle-test experiments. *Phys. Rev. A*, 90:023609, Aug 2014.
57. B Barrett, L Antoni-Micollier, L Chichet, B Battelier, P-A Gominet, A Bertoldi, P Bouyer, and A Landragin. Correlative methods for dual-species quantum tests of the weak equivalence principle. *New Journal of Physics*, 17(8):085010, aug 2015.
58. M. Kasevich and S. Chu. Measurement of the gravitational acceleration of an atom with a light-pulse atom interferometer. *Applied Physics B*, 54(5):321–332, May 1992.
59. Paul R Berman and Vasilii Kharchenko. Atom interferometry, 1997.
60. Anne Louchet-Chauvet, Tristan Farah, Quentin Bodart, André Clairon, Arnaud Landragin, Sébastien Merlet, and Franck Pereira Dos Santos. The influence of transverse motion within an atomic gravimeter. *New Journal of Physics*, 13(6):065025, jun 2011.
61. Savas Dimopoulos, Peter W. Graham, Jason M. Hogan, and Mark A. Kasevich. General relativistic effects in atom interferometry. *Phys. Rev. D*, 78:042003, Aug 2008.
62. A. Gauguet, T. E. Mehlstäubler, T. Lévêque, J. Le Gouët, W. Chaibi, B. Canuel, A. Clairon, F. Pereira Dos Santos, and A. Landragin. Off-resonant raman transition impact in an atom interferometer. *Phys. Rev. A*, 78:043615, Oct 2008.
63. C Schubert, J Hartwig, H Ahlers, K Posso-Trujillo, N. Gaaloul, U. Velte, A. Landragin, A. Bertoldi, B. Battelier, P. Bouyer, F. Sorrentino, G. M. Tino, M. Krutzik, A. Peters, S. Herrmann, C. Lämmerzahl, L. Cacciapouti, E. Rocco, K. Bongs, W. Ertmer, and E. M. Rasel. Differential atom interferometry with ^{87}Rb and ^{85}Rb for testing the uff in ste-quest. [arXiv:1312.5963](https://arxiv.org/abs/1312.5963).
64. A Peters, K Y Chung, and S Chu. High-precision gravity measurements using atom interferometry. *Metrologia*, 38(1):25–61, feb 2001.
65. B. Dubetsky. Full elimination of the gravity-gradient terms in atom interferometry. *Applied Physics B*, 125(10):187, September 2019.
66. P. Cheinet, B. Canuel, F. Pereira Dos Santos, A. Gauguet, F. Yver-Leduc, and A. Landragin. Measurement of the Sensitivity Function in a Time-Domain Atomic Interferometer. *IEEE Trans. Instrum. Meas.*, 57(6):1141–1148, 2008.
67. C. Ufrecht. Theoretical approach to high-precision atom interferometry. PhD thesis, Universitt Ulm, 8 2019.
68. G. Salomon, L. Fouché, S. Lepoutre, A. Aspect, and T. Bourdel. All-optical cooling of ^{39}K to bose-einstein condensation. *Phys. Rev. A*, 90:033405, Sep 2014.
69. S. Abend *et al.*. Atom-chip fountain gravimeter. *Phys. Rev. Lett.*, 117:203003, 2016.
70. S. S. Szigeti, J. E. Debs, J. J. Hope, N. P. Robins, and J. D. Close. Why momentum width matters for atom interferometry with bragg pulses. *New J. Phys.*, 14(2):023009–, 2012.
71. Étienne Wodey, Dorothee Tell, Ernst M. Rasel, Dennis Schlippert, Roger Baur, Ulf Kissling, Beat Kölliker, Michael Lorenz, Mark Marrer, Urs Schläpfer, Mischa Widmer, Christian Ufrecht, Stefan Stuiber, and Peter Fierlinger. A scalable high-performance magnetic shield for Very Long Baseline Atom Interferometry. [arXiv:1911.12320](https://arxiv.org/abs/1911.12320).
72. J. Rudolph. Matter-Wave Optics with Bose-Einstein Condensates in Microgravity. Phd thesis, Leibniz Universität Hannover, 2016.
73. T. Kovachy, J. M. Hogan, A. Sugarbaker, S. M. Dickerson, C. A. Donnelly, C. Overstreet, and M. A. Kasevich. Matter wave lensing to picokelvin temperatures. *Phys. Rev. Lett.*, 114:143004, 2015.
74. H. Müntinga, H. Ahlers, M. Krutzik, A. Wenzlawski, S. Arnold, D. Becker, K. Bongs, H. Dittus, and H. Duncker *et al.*. Interferometry with Bose-Einstein Condensates in Microgravity. *Phys. Rev. Lett.*, 110:093602, 2013.
75. M. Gebbe et al. Twin-lattice atom interferometry. [arXiv:1907.08416](https://arxiv.org/abs/1907.08416), 2019.
76. B. Plotkin-Swing, D. Gochnauer, K. E. McAlpine, E. S. Cooper, A. O. Jamison, and S. Gupta. Three-Path Atom Interferometry with Large Momentum Separation. *Phys. Rev. Lett.*, 121:133201, 2018.
77. M. Jaffe, V. Xu, P. Haslinger, H. Müller, and P. Hamilton. Efficient Adiabatic Spin-Dependent Kicks in an Atom Interferometer. *Phys. Rev. Lett.*, 121:040402, 2018.
78. K. Kotru, D. L. Butts, J.M. Kinast, and R. E. Stoner. Large-area atom interferometry with frequency-swept raman adiabatic passage. *Phys. Rev. Lett.*, 115:103001, 2015.
79. G. D. McDonald, C. C. N. Kuhn, S. Bennetts, J. E. Debs, K. S. Hardman, J. D. Close, and N. P. Robins. *Eur. Phys. Lett.*, 105:63001, 2014.
80. Sheng-wei Chiow, Tim Kovachy, Hui-Chun Chien, and Mark A Kasevich. $10^2 \hbar k$ large area atom interferometers. *Phys. Rev. Lett.*, 107(13):130403, 2011.
81. Sheng-wei Chiow, Sven Herrmann, Steven Chu, and Holger Müller. Noise-immune conjugate large-area atom interferometers. *Phys. Rev. Lett.*, 103(5):050402, 2009.
82. P. Cladé, S. Guellati-Khélifa, F. Nez, and F. Biraben. *Phys. Rev. Lett.*, 102:240402, 2009.
83. Sascha Kulas, Christian Vogt, Andreas Resch, Jonas Hartwig, Sven Ganske, Jonas Matthias, Dennis Schlippert, Thijs Wendrich, Wolfgang Ertmer, Ernst Maria Rasel, Marcin Damjanic, Peter Weßels, Anja Kohfeldt, Erdenetsetseg Luvsandamdin, Max Schiemangk, Christoph Grzeschik, Markus Krutzik, Andreas Wicht, Achim Peters, Sven Herrmann, and Claus Lämmerzahl. Miniaturized lab system for future cold atom experiments in microgravity. *Microgravity Science and Technology*, 29(1):37–48, Feb 2017.

84. Christian Vogt, Marian Woltmann, Sven Herrmann, Claus Lämmerzahl, Henning Albers, Dennis Schlippert, and Ernst M. Rasel. Evaporative cooling from an optical dipole trap in microgravity. Phys. Rev. A, 101:013634, Jan 2020.
85. D. Becker *et al.*. Space-borne BoseEinstein condensation for precision interferometry. Nature, 562:391, 2018.
86. G. M. Tino *et al.*. Precision Gravity Tests with Atom Interferometry in Space. Nucl. Phys. B (Proc. Suppl.), 243-244:203–217, 2013.